Navigating the 18-*n*+*m* Isomers of $PdSn_2$: Chemical Pressure Relief through Isolobal Bonds and Main Group Clustering

Amber Lim and Daniel C. Fredrickson*

Department of Chemistry, University of Wisconsin-Madison, 1101 University Avenue, Madison, Wisconsin, 53706, United States

ABSTRACT: The 18-*n* electron counting rule provides structural guidelines for electronically feasible transition metal (T) – main group (E) phases, contributing towards the goal of materials design. However, the availability of numerous potential structure types at any electron count creates a challenge for the prediction of the preferred structures of specific compounds, as is illustrated by the concept of 18-*n*+*m* isomerism. In this Article, we explore the driving forces stabilizing one 18-*n*+*m* isomer over another with an analysis of the structure of $PdSn_2$, a layered intergrowth of the fluorite and $CuAl_2$ structure types. The DFT-reversed approximation Molecular Orbital (DFT-raMO) method reveals that $PdSn_2$ and its hypothetical parent structures all adhere to bonding schemes approximating the electronic configurations expected from the 18-*n* rule, with various degrees of isolobal Pd-Pd bonding and Sn clustering. However, partial electron transfer between the Pd 5p orbitals to the Sn 5s orbitals contributes to the absence of convincing electronic pseudogaps near their Fermi energies. As such, there is no clear electronically driven preference among the structure types. This situation allows for atomic packing effects to prevail: DFT-Chemical Pressure (DFT-CP) analysis illustrates that in the fluorite-type parent structure, positive Pd-Sn CPs lead to over-compression of the Pd atoms and a stretching of the relatively open Sn sublattice. In contrast, in the $CuAl_2$-type parent structure, Sn atoms cluster into tetrahedra, opening space for an expanding Pd environment and the formation of Pd-Pd interactions. However, the tetrahedral packing of the Sn atoms here leads to frustration between negative and positive Sn-Sn CPs. Through the development of the angular CP correlation function (CP_{cor+}) as a tool to quantify frustration among interatomic interactions, we demonstrate how the observed $PdSn_2$ structure balances these effects by tuning the degree of Sn-Sn clustering and expansion of the Pd environment. These observations point to generalizations for most 18-*n*+*m* isomers, where increased main group ligand clustering (+*m*) and isolobal bonds (+*n*) can accommodate compositions with different T and E atomic sizes.

1. INTRODUCTION

The Hume-Rothery factors—electronics,[1-10] atomic packing,[11-17] and electronegativity[16-20]—shape our understanding of how a metallic material is stabilized. While most attention is given to systems in which one of these factors dominates, Hume-Rothery himself highlights the potential for these factors to interact in the stability ranges of some materials.[21] Transition metal (T)-main group (E) systems set up such a case. In intermetallic phases on the E-rich sides of these systems, each T atom is expected to achieve closed-electron configurations at 18-*n* electrons,[22] where *n* is the number of electron pairs it covalently shares with other T atoms. However, for any given electron count, there are numerous structures that can fulfill this requirement, especially when we consider changes in *n* being coupled to the transfer of electrons between the T and E sublattices. We term this diversity of structural possibilities 18-*n*+*m* isomerism.[23] With so many electronically viable options, other factors such as atomic size ratios can become decisive in determining the observed structure for any given compound. In this Article, we explore how such interactions underlie the observed structure of $PdSn_2$, with broader lessons for 18-*n* compounds.

The 18-*n* electron-counting rule broadly links atomic T-T connectivity with the valence electron concentration.[22] T atoms may obtain closed-shell electronic configurations through the sharing of electrons in multicenter T-T bonding functions isolobal to classical two-center two electron bonds (or as recently demonstrated, three-center two-electron bonds),[24] referred to as *isolobal bonds*. Any number of electrons not associated with the T atoms are found in E-based bonds or clusters secluded from the T atoms. The electronics are described with an 18-*n*+*m* bonding scheme, where *n* and *m* define the number of electrons shared in isolobal bonds and E-based bonding functions, respectively. The number of structures encompassed by this scheme is potentially substantial: a preliminary search of the Inorganic Crystal Structure Database reveals 519 experimentally realized binary T-E intermetallics that form in 126 unique 18-*n*+*m* structure types, in addition to numerous ternary phases and solid solutions.[25-30]

However, various possible (*n*,*m*) configurations and corresponding structure types may be proposed for any given composition and electron count. How do systems navigate all the possible 18-*n*+*m* isomers to find the most stable structure? In our recent investigations of 18-*n*+*m* isomerism in $REAl_3$ phases (RE = lanthanide or group 3 metal) and $IrIn_3$, we observed that competition between electronic and atomic packing effects strongly influences which isomer is favored.[23,31,32] While explanations for these cases of 18-*n*+*m* isomerism have been offered, predictive guiding principles for the design in these materials are still limited. Achieving these goals requires broader consideration of the driving forces and structural mechanisms for increasing or decreasing the *n* and *m* values for a compound.

For this purpose, we explore $PdSn_2$ as a model system. $PdSn_2$ forms in its own type (*tI*48) and can be described as an intergrowth of alternating layers of the fluorite (CaF_2) type and the $CuAl_2$-type structures along the *c* axis (Figure 1).[33-35] (A shorter stacking variant of the intergrowth structure is also experimentally realized with the

$CoGe_2$ type.[36]) The parent CaF_2 type is built from a primitive cubic network of E atoms, with a T atom at the center of every other cubic void (Figure 1). The other parent structure, the $CuAl_2$ type ($tI12$), is composed of chains of T-centered square antiprisms (derived from the primitive cubic E sublattice in the CaF_2 type by distorting square nets into 43^243 nets) stacked along the *c*-axis. When these two structure types intergrow, the $CuAl_2$ type is sliced into slabs, where the Pd-centered square antiprisms occur in pairs buffered by distorted Sn tetrahedra. These slabs are terminated by a shift in the Pd-Pd patterning that is representative of the CaF_2 type.

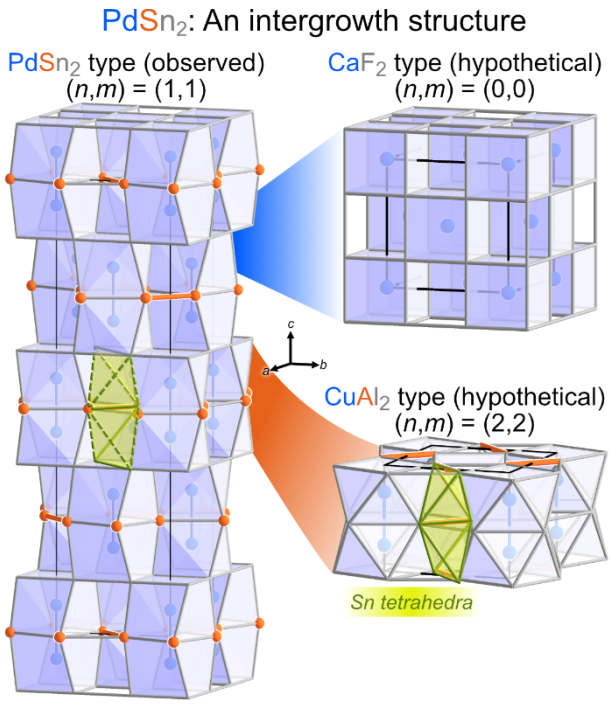

Figure 1. The $PdSn_2$ structure type, viewed as an intergrowth of the CaF_2 and $CuAl_2$ types. These three structures are 18-*n*+*m* isomers, but of these, only the $PdSn_2$ type (along with its stacking variant, the $CoGe_2$ type) is experimentally observed for $PdSn_2$. Isolobal bonds (counted by *n*) between Pd atoms are represented by blue cylinders while Sn atoms are shown in gray and orange, with orange cylinders denoting Sn-Sn interactions related to the electrons accounted for with *m*. Examples of Sn tetrahedra are highlighted in yellow.

From structural inspection, these structures appear to be 18-*n*+*m* isomers of each other: the number of Pd-Pd bonds (*n*) varies across these related structure types, with corresponding changes in the Sn-Sn connectivity. We consider the 18-*n*+*m* scheme for the CaF_2 type: the Pd atoms are too distant for isolobal bonding (4.52 Å), resulting in an initial assignment of the *n*=0 isolobal bonds. Since the valence electron count is 18 electrons, following the 18-*n* rule, no electrons should be associated with Sn-based bonding functions (*m*=0). In contrast, the Pd atoms of the $CuAl_2$ type are arranged in chains; each Pd atom can share one electron per Pd-Pd contact along the *c*-axis for a total of *n*=2. The distorted Sn tetrahedra buffering these square antiprisms (yellow) could also host electrons, where the shortest Sn-Sn contacts in these tetrahedra lie in *ab* planes, bridging $Pd@Sn_8$ square antiprisms (orange cylinders, Figure 1). Each Sn atom is involved in one such Sn-Sn interaction. Single bonds at each contact would then correspond to 2 electrons/formula unit, and thus 2 electrons/Pd atom. Accordingly, we assign the (*n*,*m*) configuration of the $CuAl_2$ type as (2,2).

Naturally, the intergrowth $PdSn_2$ structure type is assigned an intermediate (*n*,*m*) configuration. Pd atoms are paired in $CuAl_2$-type slabs, forming one isolobal bond per Pd atom. Additionally, short Sn-Sn contacts that could host electrons, like the ones in the $CuAl_2$ type, appear in these slabs (orange cylinders). At the interfaces of these slabs, the CaF_2 type interrupts the Pd-Pd connectivity, reducing the number of isolobal bonds and short Sn-Sn contacts (relative to the $CuAl_2$ type) by half. Consequently, the (*n*,*m*) configuration of the $PdSn_2$-type form is (1,1), in-between the configurations assigned to its parent structure types.

Remarkably, only the intergrowth structure types ($PdSn_2$ and $CoGe_2$ types) have been synthesized for $PdSn_2$; the parent structure types remain hypothetical. How do the electronic configurations and packing effects drive the preference for the (*n*,*m*) = (1,1) configurations over its parent structure types?

In this Article, we will see how none of the electronic configurations of the three possible structures are strongly favored over the others, allowing atomic packing effects to dominate. Using DFT-Chemical Pressure (CP) analysis and a new metric of packing frustration, the angular CP correlation function (CP_{cor+}), we will delve into the opposing desires for expansion or contraction among the interatomic contacts in these structures. From this study, we will arrive at a picture for how the observed structures of $PdSn_2$ are preferrable to the simpler alternatives, as well as more general structural mechanisms by which changes in isolobal bond counts (*n*) and clustering of E atoms (*m*) balance the atomic size requirements of the T and E sublattices in intermetallics governed by the 18-*n* bonding scheme.

2. EXPERIMENTAL SECTION

2.1 Electronic Density of States. Electronic density of states (DOS) distributions for $PdSn_2$ in the CaF_2, $PdSn_2$, and $CuAl_2$ structure types were calculated with the Vienna Ab-initio Simulation Package (VASP) using the generalized gradient approximation (GGA) functionals with the Perdew-Burke-Ernzehof (PBE) parameterization and the corresponding Projector Augmented Wave potentials provided with the package.[37-41] The structures were geometrically optimized in a two-step method: first, the atomic positions were released while the cell was held constant, then both atomic positions and cell parameters were relaxed. An energy cutoff of 330 eV was used for all calculations in the accurate-precision mode with Γ-centered k-point meshes (7×7×7 for the CaF_2 and $CuAl_2$ types; 5×5×5 for the $PdSn_2$ type). The calculations were considered converged at energy differences of 10^{-5} eV between electronic steps and 10^{-4} eV between ionic steps. Single-point calculations were performed on the geometry-optimized structure at finer *k*-point meshes to obtain convergence in the features of the density of states (DOS) distributions. Detailed computational parameters, including *k*-point meshes, are listed in the Supporting Information.

2.2 DFT-raMO analysis. Static calculations for each system were performed using the optimized geometries obtained from VASP. To obtain wavefunctions over the whole Brillouin zone, calculations were performed without symmetry considerations, using a Γ-centered 2×2×2 *k*-point mesh for CaF_2- and $CuAl_2$-type $PdSn_2$, and a 2×2×1 *k*-point mesh for $PdSn_2$-type $PdSn_2$. The resulting wavefunctions were imported into the *DFT-raMO.jl* package.[42] In each cycle of the analysis, overlap integrals between the current basis set of occupied functions and the target function (constructed from a linear combination of Slater-type orbitals parameterized to approximate the corresponding PAW projector function)[43] was calculated and subsequently used to generate the raMO Hamiltonian matrix for the target. The matrix was then diagonalized to obtain a reconstructed version of the target

function as well as remainder functions, which were returned to the basis set and used for regenerating subsequent targets.

2.3. DFT-Chemical Pressure Analysis. The DFT-Chemical Pressure (CP) schemes were calculated with the ABINIT software package, using the local density approximation (LDA) and Hartwigsen-Goedecker-Hutter (HGH) norm-conserving pseudopotentials (the standard platform for DFT-CP calculations).[44-48] All structures were geometrically optimized using an analogous two-step method to that described in 2.1 for the VASP calculations. Optimizations were considered converged when the energy differences were below 10^{-5} eV between two electronic steps and when the magnitude of the net force on each atom is less than 2.6×10^{-3} eV/Å for the ionic steps. The energy cutoff was set to 40 Ha, while Γ-centered 9×9×9 and 5×5×5 k-point meshes were used for the parent structure types (CaF_2 and $CuAl_2$) and intergrowth $PdSn_2$ structure types, respectively.

Static calculations at the equilibrium, slightly contracted, and slightly expanded geometries (linear scale ±0.5%) were performed to obtain electron densities, kinetic energy densities, and local components of the Kohn-Sham potentials. CP maps were then constructed using the core-unwarping procedure, with contributions from the Ewald energy and E_α components being spatially distributed to achieve self-consistency between net pressures obtained from contact volumes and atomic cells, as obtained from an iterative binary Hirshfeld (ibH) scheme,[49,50] with the Atomic Pseudo-potentials Engine (APE) being called for the necessary free ion calculations.[51] In this process, it was found that trends and internal consistency of the CP schemes depended on the electron configuration for the free-ion Pd calculations. For the schemes presented here, the ibH charge determinations were initialized with the Pd configuration $5s^1\,4d^9$ (as opposed to the default of $5s^0 4d^{10}$), with the 4d orbital accommodating any additional electrons that were added over the course of the process; the results are very similar if the 5s orbital is used to accommodate these electrons. The pressures within contact volumes were averaged and projected onto spherical harmonics centered on each atomic site.[52] The CP schemes were visualized with spherical harmonics up to $l_{max} = 4$, using the in-house program figuretool2.

3. RESULTS & DISCUSSION

3.1 The electronic density of states of $PdSn_2$. The 18-*n* rule for T-E intermetallics links electron count to structural connectivity. In this scheme, the T atoms are envisioned as reaching closed-shell configurations through the sharing of *n* electron pairs in multicenter T-T bonding functions. The rule also leaves margin for a number of electrons (*m* per T atom) to inhabit bonding functions not associated with the T atoms, typically in 2c-2e bonds, clusters, or other multicentered functions. The corresponding electronic configuration is termed the 18-*n*+*m* bonding scheme. Though the 18-*n* rule provides an approach to describing the electronic structure of T-E intermetallics, on its own, it is not prescriptive: many 18-*n*+*m* bonding configurations exist for any given electron count, i.e. 18-*n*+*m* isomers.

$PdSn_2$ provides a promising case for studying preferences among 18-*n*+*m* isomers, as it appears to represent a transition point between two simpler parent (*n*,*m*) isomers. Most compounds adopting the $PdSn_2$ type have valence electron concentrations between 17.22 and 18 electrons per T atom, (with one exception at 20.72 electrons/T), suggesting a narrow range of electronic stability.[53-57] At a valence electron count of 18 electrons/Pd atom, the observed structure of $PdSn_2$ has an apparent (*n*,*m*) configuration of (1,1), while the hypothetical CaF_2- and $CuAl_2$-type forms would have configurations of (0,0) and (2,2), respectively.[22] How well do these assignments capture the bonding in these competing structures?

We begin with an electronic analysis to assess the validity of these bonding schemes and the (*n*,*m*) assignments. The total energies calculated for the three structures indicate that the $PdSn_2$ type is the preferred structure type (see the Supporting Information). However, while the total energy for the $CuAl_2$ type is 0.103 eV/formula unit higher, the value for the CaF_2 type is only barely outcompeted by the $PdSn_2$ type, by 5.00×10^{-3} eV/formula unit. This trend of E($PdSn_2$ type) ~ E(CaF_2 type) < E($CuAl_2$ type) is found for both PBE-DFT and LDA-DFT.

At the ideal (*n*,*m*) configurations, the Pd atoms in each structure should achieve closed shell configurations through the population of functions centered on individual T atomic orbitals, isolobal bonds (*n*), and main group-based cluster orbitals (*m*). The resulting electronic stability is typically correlated to the occurrence of a gap or pseudogap at the Fermi energy (E_F) in the electronic density of states (DOS) distributions.

However, calculations of the DOS distributions of $PdSn_2$ in the three phases (Figure 2) indicate that this system does not fall into that category. Each DOS distribution is relatively flat near the E_F, with faint minima being discernable for CaF_2 and $PdSn_2$, as noted previously in an electronic structure study of $PdSn_2$ and its Sn-rich relatives in the Pd-Sn system.[35] The shallowness of these variations is indicative of metallic character. These results are consistent with a recent study of the band structure of $PdSn_2$, which concludes the phase has metallic behavior, with hole and electron pockets near the Fermi energy (E_F).[58] The holes are primarily attributed to Sn 5p bands, while electron pockets have Sn 5s, $5p_x$, and $5p_y$ contributions.

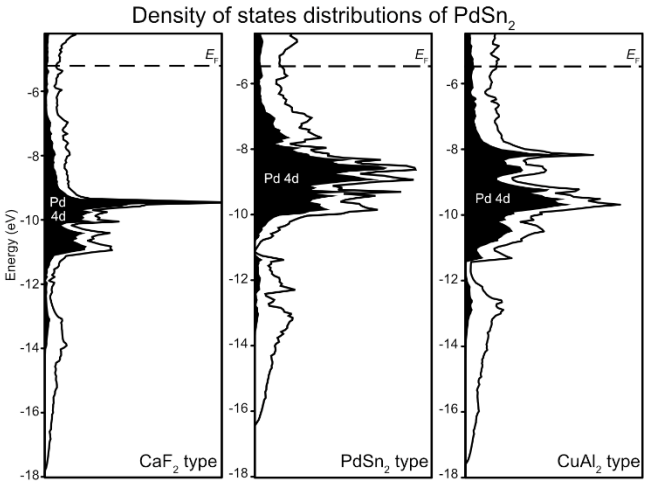

Figure 2. Electronic density of states (DOS) distributions of $PdSn_2$ in the CaF_2, $PdSn_2$, and $CuAl_2$ structure types, from left to right. Contributions to the DOS from the Pd 4d orbitals are shaded in black.

Such a situation, however, does not mean that 18-*n*+*m* picture is inapplicable, just as some Zintl phases also lack pseudogaps but exhibit structures perfectly in-line with the Zintl scheme.[10,59,60] We note that the absence of striking pseudogaps at the Fermi energy in the DOS distributions also has precedence in some 18-*n*+*m* compounds, which nonetheless have bonding interpretable in terms of 18-*n*+*m* configurations. An obscured pseudogap can arise from the presence of unanticipated isolobal bonds, as in Ni_3Sn-type YAl_3,[32] T–T π-bonding in $TiAl_3$,[22] or the unexpected population of main group-based cages, as seen in $IrIn_3$-type $IrIn_3$[23] and $IrAl_4$.[61] In these cases, the Fermi energies were misaligned with respect to the nearest pseudogap. We will see in the next section how $PdSn_2$ is another

example, with the 18-*n*+*m* scheme still providing a guide to the electronic structure.

3.2. DFT-raMO analysis of $PdSn_2$-type $PdSn_2$. To examine whether the various plausible structures of $PdSn_2$ represent competing 18-*n*+*m* isomers, we perform DFT-reversed approximation Molecular Orbital analysis (DFT-raMO).[43] DFT-raMO uses the occupied crystal orbitals obtained from a DFT calculation as a basis set for the reconstruction of localized molecular orbital-like target functions. These reconstructions (raMOs) resemble Wannier functions[62,63] as linear combinations of crystal orbitals across the Brillouin zone. The quality of the raMOs is then assessed; if the raMOs exhibit expected angular characteristics and relative localization, electrons are sequentially assigned to the targeted functions. Otherwise, the raMOs are rejected and returned to the basis set, and new hypotheses and target functions are formulated. DFT-raMO thus produces a molecular-like electronic scheme that accounts for all the electrons in the system, providing a direct means to validate a proposed bonding scheme.

In our approach to creating the DFT-raMO schemes for each of the competing structures for $PdSn_2$, we attempt to reconstruct the most contracted valence orbitals of the Pd atom first (Pd 4d), then move to more diffuse orbitals (Pd 5s, 5p, and any isolobal bonds based on them), and then Sn based orbitals (Sn-Sn bonding functions, if expected, and then individual 5s and 5p atomic orbitals).[64] DFT-raMO schemes for all three structures revealed bonding interpretable in terms of the 18-*n*+*m* scheme.

The raMOs for the observed structure of $PdSn_2$ (Figure 3) are representative of the results obtained for the three structure types. The 4d atomic orbitals of the Pd atom are relatively contracted and fully occupied, accounting for 10 electrons/Pd atom. The Pd 5s raMOs are also well-constructed but appear more diffuse; these orbitals account for another 2 electrons/Pd atom. Similarly, a Pd-Pd isolobal bond can be reconstructed for each Pd_2 dumbbell, using as targets in-phase combinations of the Pd $5p_z$ orbitals supplemented with bridging Sn contributions. For the isolobal bond raMOs, the representative isosurfaces show multicenter interactions, with major contributions from squares of Sn atoms bisecting the Pd-Pd interaction (green surface) and capping the Pd antiprism units (light blue surfaces). Prominent back lobes are also present (light blue), which is consistent with the use of Pd $5p_z$ orbitals in the target functions.

The 18-electron configuration on the Pd atoms would then be completed by the filling of the Pd $5p_x$ and $5p_y$ orbitals with 4 electrons/Pd atom. However, the Pd $5p_x$ and $5p_y$ orbitals are only partially filled at 3.5 electrons in total, suggesting a depopulation of antibonding π^* interactions between the Pd 5p orbitals (see the Supporting Information for a comparison of the π and π^* reconstructions).

Next, we turn to the raMO functions for the Sn-Sn bonds in the $CuAl_2$-type layers, the proposed home of the *m*=1 electrons in the (*n*, *m*) = (1,1) scheme. These appear with a diffuse blue ovoid encompassing the Sn_2 pair, with smaller out-of-phase contributions on the neighboring Sn atoms (which likely play the role of orthogonalizing the Sn-Sn bonding functions from each other). These Sn-Sn bonds in the $CuAl_2$-type layers account for 0.97 electrons/Pd atom, just shy of the predicted *m*=1 count. The structure's remaining 0.53 electrons are found in delocalized Sn 5s-based functions.

Altogether, the raMO results $PdSn_2$ in its own type can be summarized with an effective (*n*,*m*) configuration of (1.5, 1.5), with the non-integer values resulting from the transfer of 0.5 electrons from the Pd to the Sn. The corresponding schemes for the CaF_2 and $CuAl_2$ type, described in sections S2 and S3 of the Supporting Information, can be understood in similar terms. For the CaF_2 type, the expected (*n*,*m*) = (0, 0) is reflected in the near complete reconstruction of the Pd spd valence atomic orbitals to approximate filled 18-electron configurations. However, partial electron transfer from the Pd 5p orbitals to the Sn 5s leads to an approximate configuration of (0.25, 0.25). In terms of the $CuAl_2$ type, the expected isolobal bonds and Sn-Sn bonds for the (1,1) configuration are obtained, but the *n* and *m* are 0.5 electrons larger than expected, arising again from the transfer of electrons from the Pd $5p_x$ and $5p_y$ orbitals.

The consistent pattern of electron transfer between the nominally closed-shell Pd atoms and the Sn (larger for the $CuAl_2$ and $PdSn_2$ types presumably due to the presence of Pd-Pd π^* orbitals) contributes to the absence of a clear electronic driving force favoring the formation of these potential structures for $PdSn_2$ over the others, with each representing a plausible 18-*n*+*m* isomer. How does the system select which structure type to form? As we will see in the next section, the presence of isolobal bonds and main group clusters have ramifications for the atomic packing for transition metal and main group atoms that shapes the preferences among the structures.

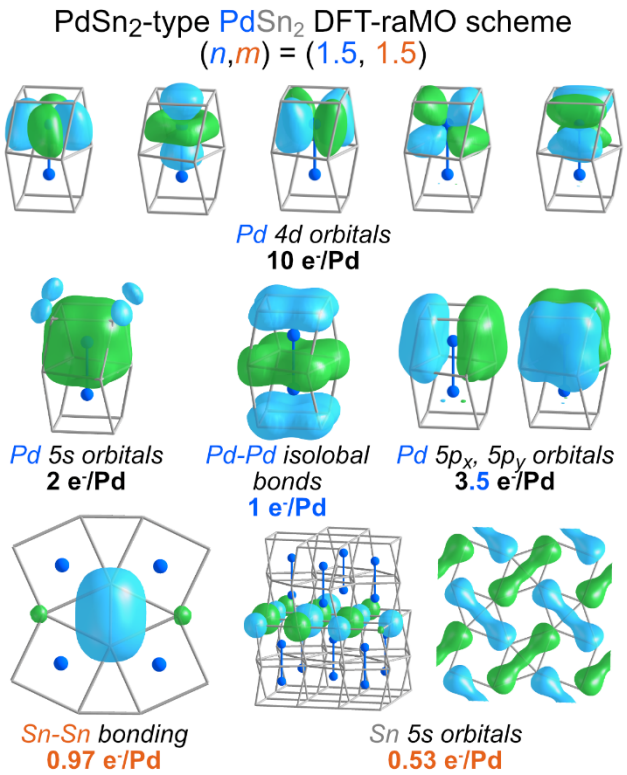

Figure 3. DFT-raMO scheme for $PdSn_2$ in its own type, summarized with representative raMO functions. The raMOs corresponding to the valence atomic orbitals of the Pd atoms are nearly full, except for the Pd $5p_x$ and $5p_y$ orbitals. Pd-Pd isolobal bonds account for 1 electron/Pd atom, while Sn-based states account for 1.5 electrons, leading to an (*n*,*m*) configuration of (1.5, 1.5). Corresponding schemes for hypothetical CaF_2- and $CuAl_2$-type forms of $PdSn_2$ are presented in the Supporting Information.

3.3 DFT-Chemical Pressure Analysis. As electronic effects seem to only weakly influence the relative stabilities of the competing 18-*n*+*m* isomers for $PdSn_2$, we now consider the potential effects of the atomic packing component. We begin by comparing the overall packing efficiencies of these plausible (*n*,*m*) isomers of $PdSn_2$. The calculated densities for optimized geometries of the three structures are tabulated in Table 1. From LDA-DFT calculations, the CaF_2 type occupies the most volume per formula unit at 65.43 $Å^3$/f.u., while the $CuAl_2$ type is the densest at 60.55 $Å^3$/f.u. Similar observations are made with PBE-GGA-DFT calculations. This trend is understandable from the presence of cubic voids in the former, while all the interstitial spaces in the latter are within distorted tetrahedra. The $PdSn_2$ type, as an intergrowth of the two other types, has an intermediate density.

From the differences in local geometry of these structure types and their densities, we can anticipate problems in the atomic packing in the parent structures. The larger void spaces in the CaF_2 type could be unfavorable in terms of packing efficiency, while tetrahedral close packings, such as that found in the $CuAl_2$ type, face the geometrical impossibility of filling space with ideal tetrahedra.[65] An intergrowth of the two types, as provided by the $PdSn_2$ structure type, may provide a less strained arrangement.

Table 1. Calculated volume per formula unit ($Å^3$/f.u.)

Structure type	LDA	PBE
CaF_2 type	65.43	69.97
$PdSn_2$ type	62.75	67.31
$CuAl_2$ type	60.55	64.56

To analyze these effects, we performed DFT-Chemical Pressure (CP) analysis on $PdSn_2$ in the three structure types, yielding the CP schemes shown in Figure 4. The CP features on each atom are presented with radial plots whose surfaces represent the chemical pressure experienced along different directions, with the signs of the pressure denoted by the surface color. White lobes denote positive pressure, where contacts are too short and would be relieved from an expansion of the structure. Conversely, black lobes represent negative pressures, where contacts are too long and would be relieved by contraction. Note that as these structures are geometrically optimized, their overall internal pressures are each 0; the CPs emphasize how this net situation emerges from competing interactions at different interatomic contacts.

We begin our analysis with the CP scheme of CaF_2-type $PdSn_2$. Each Pd atom is encased in a white, cubic CP distribution whose lobes point towards the Sn atoms in the first coordination sphere at 2.77 Å. These positive pressures between the Pd and Sn atoms indicate that the Pd atom is too large for its coordination environment. These tensions would be soothed by an expansion of the structure. However, expansion is resisted by negative CP features along the Sn-Sn contacts (shortest distances: 3.20 Å). The Sn network is already overly extended and instead would benefit from shorter interatomic distances. The overall result is a frustrated packing situation.

Let's turn now to the other parent structure, $CuAl_2$-type $PdSn_2$ (Figure 4b). The Pd atoms, highlighted in blue, are decorated with d_{z^2}-shaped CP distributions, with a dumbbell of large negative CP lobes directed along **c** and a torus of positive CP around the equator. The relatively large negative CPs are aligned along Pd-Pd contacts (2.86 Å). However, the desire for shorter contacts here is limited by

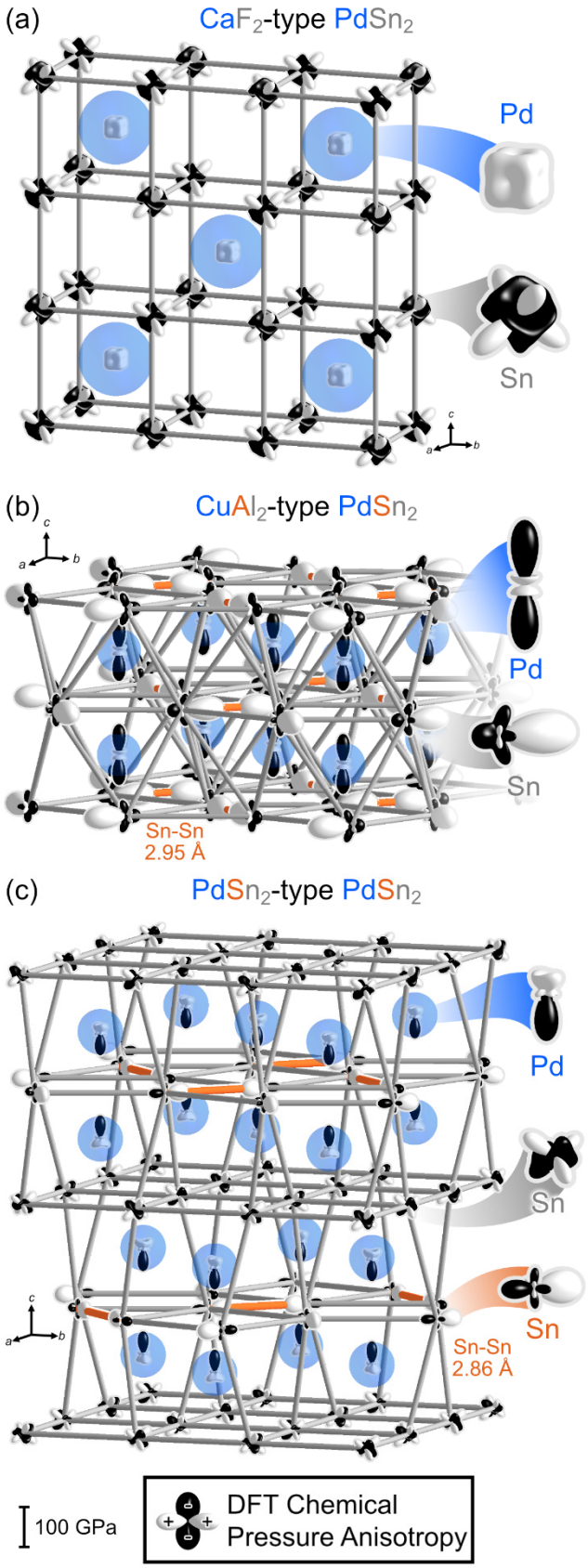

Figure 4. DFT-Chemical Pressure schemes calculated for $PdSn_2$ in the (a) CaF_2, (b) $CuAl_2$, and (c) $PdSn_2$ types. The shortest Sn-Sn interactions in the $CuAl_2$- and $PdSn_2$ -type structures are denoted with orange cylinders. Enlarged versions of the CP distributions are shown to the right for one instance of each symmetry distinct site.

positive Pd-Sn CPs and the fact that each Pd atom is pulled in opposite directions by its negative CP lobes. Altogether, on moving from the CaF_2-type to the $CuAl_2$ type, the positive Pd-Sn CPs have been joined by negative Pd-Pd ones, highlighting the expansion of the Pd coordination environment from 8 to 10 neighbors. This expansion is accompanied by a decrease in the net CP on the Pd atoms (CaF_2 type, +54.8 GPa; $CuAl_2$ type, +5.2 GPa) both from the reduction of the magnitude of the positive Pd-Sn CPs and the introduction of negative Pd-Pd CPs.

The strongest CP tensions for the $CuAl_2$ type, though, do not directly involve the Pd atoms. Instead, large positive CP features along the shortest Sn-Sn contacts (2.95 Å, orange) stand out in the CP scheme. These contacts correspond to the Sn-Sn bonds we identified in our raMO analysis. From the CP viewpoint, these interactions involve shorter distances than desired, which are enforced by negative pressures toward the Sn atoms in the layers above and below along the *c*-direction. While the $CuAl_2$ type provides an expanded Pd environment relative to the CaF_2 type, it appears that in condensing the Sn-Sn contacts to provide more space for the Pd has led to new packing issues. Could the intergrowth of the two parent structure types to form the observed structure resolve these issues?

The CP scheme of $PdSn_2$ in its own structure type confirms this expectation. The magnitudes of its CP features are reduced in comparison to those of the parent structures, indicating a global relief of the packing tensions. For example, the insertion of the CaF_2-type layers into the $CuAl_2$ type truncates the chains of Pd-Pd contacts to Pd_2 dumbbells, removing one negative CP lobe from each Pd atom and allowing that atom to form a shortened contact with its remaining Pd neighbor. This displacement simultaneously enables the reduction of positive CPs between the Pd atoms and the Sn atoms in the CaF_2-type layer.

However, CP relief on the Pd atoms does not fully explain the preference for the $PdSn_2$ type. In the CaF_2 type, the Pd atom has a net CP of +54.8 GPa, reflecting its overly compressed environment, while the Pd atom in the $CuAl_2$ type has a reduced net CP of +5.2 GPa, which originates from negative CPs along isolobal bonds. At first glance, the smaller CP lobes in the intergrowth $PdSn_2$ type would suggest that it has a lower net CP magnitude than either parent structure. In fact, the balance of the positive and negative pressures features on the Pd atoms leads to a net CP of +17.2 GPa, higher than those in the $CuAl_2$ type.

Perhaps then, the Sn atoms may contribute to these preferences as well, with the large positive Sn-Sn CPs that dominated the $CuAl_2$ type being a notable source of tension. In the $PdSn_2$ type, the corresponding Sn-Sn contacts continue to show positive CP, but now they are significantly reduced. At first glance, however, the appearance of relief here is surprising: the Sn-Sn contact distance at these positive CPs in the $PdSn_2$ type is 2.86 Å, which is *shorter* than that of its counterpart in the $CuAl_2$ type (2.95 Å). How can a shorter distance lead to a less positive CP?

A clue is offered by the broader context for these relatively short Sn-Sn contacts in the two structures. In the $CuAl_2$ type, this contact appears as a shared edge between two elongated Sn tetrahedra, with negative Sn CPs to the other atoms in the tetrahedra acting against the positive CPs. In the $PdSn_2$ type, the insertion of CaF_2-type layers has led to a more open Sn sublattice. The Sn atoms bearing the Sn-Sn positive CPs now have fewer Sn neighbors, which could allow shorter contacts to the remaining ones.

3.4 Frustration between interatomic CPs: The CP angular correlation (CP_{cor+}). Such effects relate to the ways the different interatomic interactions involving a common atom influence and conflict with each other, which can be difficult to estimate from a visual inspection of the CP schemes. To better explore the phenomenon of frustration between the chemical pressures of interatomic contacts, we define the CP angular correlation (CP_{cor}) function for a pair of contacts with a shared atom:

$$CP_{cor,i,j,k} = -v_{ji}v_{jk}P_{ji}P_{jk}\left(\hat{u}_{ji}\cdot\hat{u}_{jk}\right) \quad (1)$$

Here, the indices i, j, and k represent atoms in the structure where j is the shared atom between contacts ji and jk (Figure 5); v_{ji} is the contact volume associated with interaction between atoms i and j (as determined by the Hirshfeld-inspired assignment), P_{ji} is the corresponding chemical pressure, and $\hat{u}_{ji}$ is the unit vector pointing from atom j to atom i. The -1 factor sets the sign for convenience such that frustrated interactions correspond to positive values. With this definition, each $CP_{cor,i,j,k}$ element is a scalar with units of (volume×pressure)^2. These values can be conveniently written in terms of energy^2, but one should keep in mind they are based on volumes and pressures that play different roles: the pressures signify interatomic stresses, while the volumes weigh the relative importance of each interaction to the structure.

The level of frustration experienced by an atom can be gleaned by the sum of all positive CP_{cor} values, normalized by the number of formula units per cell, Z,

$$CP_{cor+} = \frac{1}{Z}\sum_{i,j,k} CP_{cor,i,j,k} \text{ with } CP_{cor,i,j,k} > 0 \quad (2)$$

Where the sum over i, j, and k can be over all atoms to capture a comprehensive view of a structure's frustration or tailored to include all symmetrically equivalent pairs of contacts for a feature of interest. Pairs of interactions with negative CP_{cor} values also arise, but we will pay less attention to these as they do not reveal packing tensions in themselves.

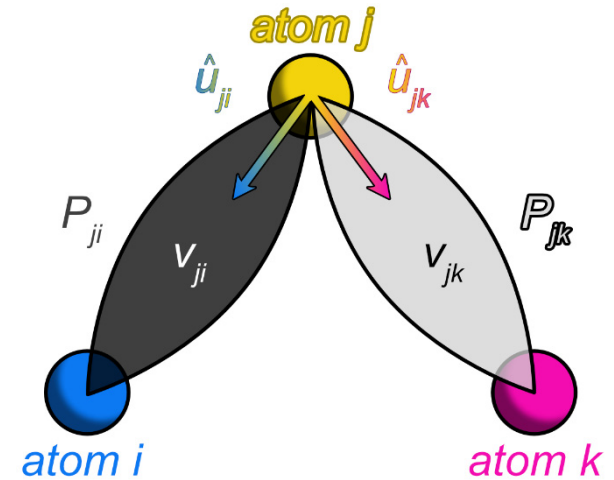

Figure 5. Schematic illustration of the parameters entered into the angular CP correlation function, CP_{cor}. See Equation 1.

Let's first illustrate this approach for a structure where the packing tensions are straightforward, CaF_2-type $PdSn_2$. A key competition in this structure is between Pd-Sn and Sn-Sn contacts. The interatomic CPs pointing from the shared Sn atom to the Pd atom are positive,

indicating a desire to expand that contact (Figure 6, top left). However, the CPs between that Sn atom to a neighboring Sn atom in the cube surrounding the Pd atom are negative, indicating a desire for a shorter contact. Because the projection of the vectors is positive, i.e. they have components that point in the same direction, the CPs of the Pd-Sn and Sn-Sn interactions contradict each other, leading to a CP_{cor+} value of 8.76 eV^2.

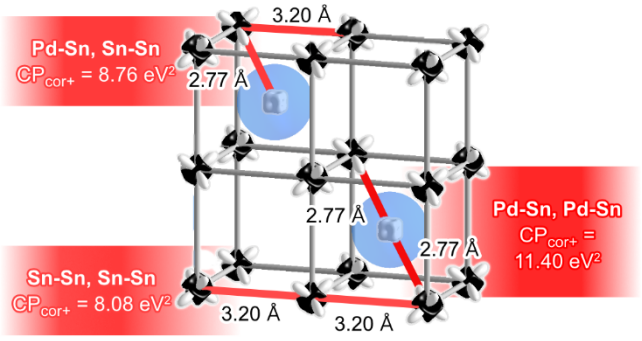

Figure 6. The CaF_2-type $PdSn_2$ CP scheme annotated with red lines for contacts corresponding to the CP_{cor+} values.

Similarly, interatomic CPs that share the same sign but point in opposite directions impart local frustration on the shared atom. This effect is observed in the Sn sublattice (Figure 6, bottom) where the negative interatomic CPs pull on the shared Sn atoms along its cubic network, which desires shrinkage (CP_{cor+} = 8.08 eV^2). The Pd atoms, however, experience even more aggravated pressures: large positive CPs point outward from the Pd atom to Sn atoms along the diagonals of the cube (Figure 6, bottom right). These positive CPs push on the Pd atom, resulting in a highly frustrated local environment. The CP_{cor+} value here for the opposing Pd-Sn contacts is 11.40 eV^2, and in fact, is the highest CP_{cor+} value per pair of interatomic interactions for all three structure types of $PdSn_2$ (see the Supporting Information for full tables of CP_{cor+} values).

We are now ready to apply this type of analysis to a comparison of the $CuAl_2$ and $PdSn_2$ types. For the $CuAl_2$ type, while the positive Pd-Sn CPs encountered in the CaF_2 type persist, these interatomic CPs are less intense and their vectors are offset by the twist of the square antiprism, leading to a CP_{cor+} value of 6.48 eV^2 (Figure 7a, ②). In addition, the large negative CPs along the chain of Pd atoms pull them in opposite directions (CP_{cor+} = 3.66 eV^2) and hinder positive Pd-Sn CPs in the same directions (CP_{cor+} = 3.24 eV^2). Clearly, a transition from the CaF_2 type to the $CuAl_2$ would not resolve all of the packing tensions around the Pd atoms.

The Sn sublattice in the $CuAl_2$ type exhibits substantial frustration as well. The aforementioned conflict between the positive CPs of the shortest Sn-Sn contact and the negative CPs of other Sn-Sn contacts that form the tetrahedra creates a CP_{cor+} value of 9.60 eV^2 (Figure 7a, ①), higher than any value found among the Pd-centered interactions. The packing situation in the $CuAl_2$ type is nearly as frustrated as that in a CaF_2-type form.

How do the packing tensions in the intermediate $PdSn_2$ type compare? Let's start with the CPs acting upon the Pd atoms. In the $PdSn_2$ type, the Pd atoms shift away from the CaF_2-type layers towards the 43^243 nets. This anisotropy in the Pd coordination environment greatly reduces the CP_{cor+} values for Pd-Sn interactions, ranging from 0.04 to 0.81 eV^2, much smaller than the corresponding CP_{cor+} values in the parent structure types (②, Figure 7b). Pd-Sn/Pd-Pd tensions are also reduced with CP_{cor+} = 0.25 to 0.26. The CP_{cor+} values associated with the Pd atom are an order of magnitude smaller in the $PdSn_2$ type than those in the CaF_2 and $CuAl_2$ types, indicating that the intergrowth structure is more suited to hosting the Pd atom.

Relief is also observed in the Sn sublattice. Recall that the Sn-Sn/Sn-Sn interactions in the $CuAl_2$ type (marked ① in Figure 7a) had significant strain. We trace the analogous interactions in the $PdSn_2$ type, where the Sn-Sn contact with the negative pressures is now 4.05 Å, much longer than the corresponding distance in the $CuAl_2$ type (3.54 Å). At this longer distance, the pull between the Sn-Sn is understandably weaker. In this manner, the lengthening of the contact reduces the influence of the negative CPs upon the Sn atom. As the weaker negative Sn-Sn CPs do not oppose the positive S-Sn CPs as much as in the $CuAl_2$ type, the CP_{cor+} value drops from 9.60 eV^2 in the $CaAl_2$ type to 0.43 eV^2.

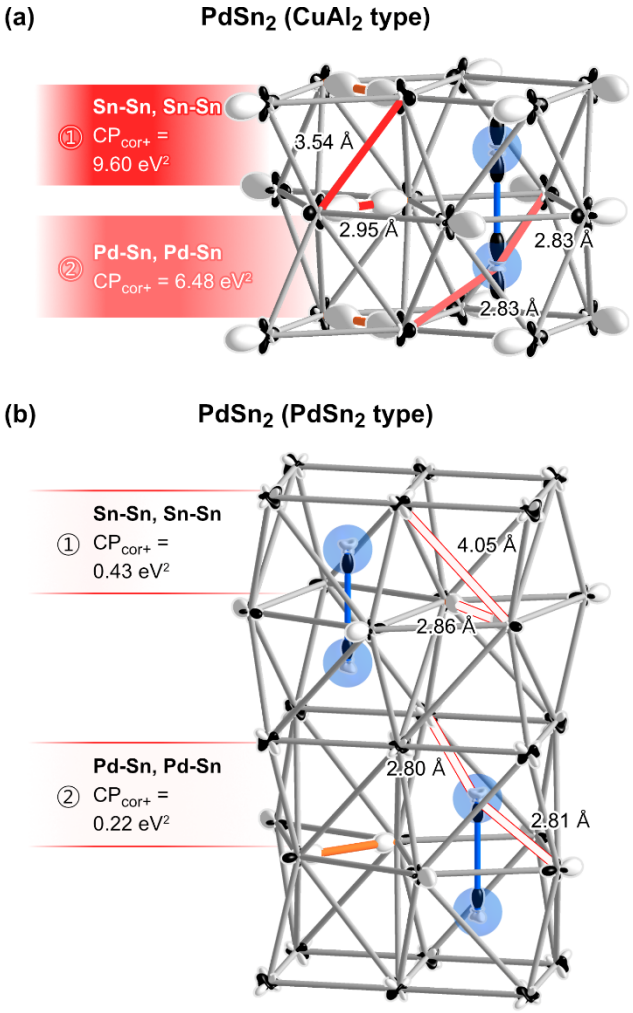

Figure 7. Key points of packing frustration in (a) $CuAl_2$- and (b) $PdSn_2$-type versions of $PdSn_2$, with the corresponding CP_{cor+} values highlighted in red.

In our DFT-Chemical Pressure analysis, we now arrive at driving forces guiding the $PdSn_2$ structure toward its observed 18-n+m isomer. In the CaF_2-type (n,m) = (0,0) form, positive CPs on the Pd atom indicate that it is too large for its environment, which leads to overly stretched Sn-Sn interactions in the Sn sublattice. The $CuAl_2$-type (2,2) form offers a solution to the positive net CPs on the Pd

atoms through the introduction of Pd-Pd isolobal bonds, which adds negative CPs onto the Pd atom site and expands the Pd coordination environments overall. The opening of space around the Pd simultaneously allows for the embedding of dedicated Sn-Sn bonding interactions in the Sn sublattice. However, the Sn-Sn clustering introduces frustrated tensions between CPs in the Sn sublattice: large negative CPs along Sn-Sn contacts between *ab* layers aggravate positive CPs within layers. It seems then, that while increasing the (n,m) configuration of the structures can open up the Pd coordination environment and shorten some Sn-Sn interactions, the $CuAl_2$-type structure represents an overreaction, as CP frustration arises among the Sn atoms.

The intergrowth $PdSn_2$ type provides a more comfortable midpoint between these extremes. The $PdSn_2$ type expands the Pd coordination environment by the presence of negative CPs along the one isolobal contact per Pd atom. Furthermore, the $PdSn_2$ type solves the tensions that would be encountered in the Sn sublattice of the $CuAl_2$ type by utilizing the CaF_2 type layers as a way to increase the distance of interlayer Sn-Sn interactions and reduce their influence on the Sn sublattice. In this way, the (n,m) configuration of $(1.5,1.5)$ granted by the $PdSn_2$ type (along with the $CoGe_2$ type, a stacking variant) emerges as the preferred 18-n+m isomer for $PdSn_2$.

4. CONCLUSIONS

In this Article, we have investigated how electronic and chemical pressure (CP) factors interact to set structural preferences among competing 18-n+m isomers, using the compound $PdSn_2$ as a model system. The 18-n rule provides (at least) three electronically feasible candidates for $PdSn_2$: the CaF_2 type $(n,m) = (0,0)$, the $CuAl_2$ type $(2,2)$, and an intergrowth of these two potential forms, the $PdSn_2$ type $(1,1)$. The electronic density of states distributions show no strong electronic preference between the structure types, while DFT-raMO analysis reveals that the 18-n+m isomers largely agree with their proposed 18-n+m bonding schemes with some additional electron transfer between the Pd and Sn.

However, CP analysis and the newly introduced CP angular correlation function, CP_{cor+}, uncover different spatial requirements for their respective (n,m) configurations. As clusters of Sn atoms increase (as in the $PdSn_2$ and $CuAl_2$ types), space opens for the Pd atoms and the formation of isolobal bonds, simultaneously increasing n and m. Increased isolobal bonding, in turn, introduces negative CPs into the Pd coordination environment, making it preferable for larger atoms. However, the Sn clustering can introduce frustrations among the increased number of interatomic contacts within Sn sublattice. In the case of the $CuAl_2$-type form $(2,2)$, large positive CPs along the shortest Sn-Sn contacts work against negative CPs along other Sn-Sn contacts.

The $PdSn_2$ structure type, as an intermediate between the CaF_2 and $CuAl_2$ types, offers a solution to these packing issues. The partial unraveling of the tetrahedral Sn atom packing in the $CuAl_2$ type allows some of the longer Sn-Sn contacts to lengthen substantially, reducing their influence on the tension between positive and negative Sn-Sn CPs. In addition, the staggering of Pd positions, corresponding to insertion of the CaF_2-type layers into the $CuAl_2$ type terminates one of each Pd atom's two Pd-Pd isolobal bonds. As a result, the remaining Pd-Pd contact can contract along the negative CPs and move away from positive CPs in the CaF_2-type layers.

These conclusions suggest some design principles for T-E intermetallics, particularly in terms of structural trends in families of 18-n+m isomers. When the T atom is relatively too large or the E sublattice is overly-stretched, an increase the (n,m) values provides a means for a system to open the T atom coordination environment and tighten E-E interactions in the sublattice. In the reverse case, if the T atoms are too small or the E atoms are over-coordinated by E neighbors, the system cleaves an isolobal bond to tighten the space around the T atom and allows a more openly packed E sublattice. Following these principles, one might devise an experiment to stabilize $PdSn_2$ in the CaF_2 type by partially substituting the Sn with Ge, a smaller E atom. We look forward to exploring how these trends apply to preferences among other 18-n+m isomers in T-E intermetallics, as well as how new bonding features such as the recently recognized 3c-2e T-T isolobal bonds[24] integrate into predictive models for these materials.

ASSOCIATED CONTENT

Optimized geometries and computational parameters for CaF_2-, $CuAl_2$-, and $PdSn_2$-type $PdSn_2$; DFT-raMO analyses for the CaF_2- and $CuAl_2$-type forms of $PdSn_2$; P_{sphere} values for the sequences of raMO reconstructions; tables of CP_{cor} values pairs of interatomic interactions. This material is available free of charge via the Internet at http://pubs.acs.org.

Interactive DFT-CP schemes and other computational details are available on the Intermetallic Reactivity Database and can be accessed through the following digital object identifiers (DOIs): $PdSn_2$ (CaF_2 type): https://doi.org/10.48704/ird_PdSn2_CaF2, $PdSn_2$ ($CuAl_2$ type): https://doi.org/10.48704/ird_PdSn2_CuAl2, $PdSn_2$ (own type): https://doi.org/10.48704/ird_PdSn2.

AUTHOR INFORMATION

Corresponding Author

Daniel C. Fredrickson – Department of Chemistry, University of Wisconsin-Madison, Madison, Wisconsin, 53706, United States; *orcid.org/0000-0002-3717-7008*; Email: danny@chem.wisc.edu

Author

Amber Lim – Department of Chemistry, University of Wisconsin-Madison, Madison, Wisconsin, 53706, United States; *orcid.org/0000-0001-9893-1740*

Notes

The authors declare no competing financial interest.

ACKNOWLEDGMENTS

We gratefully acknowledge the financial support of the National Science Foundation through Grant DMR-2127349. This research used computational resources supported by NSF grant CHE-0840494.

REFERENCES

(1) Tolman, C. A. The 16 and 18 electron rule in organometallic chemistry and homogeneous catalysis. *Chem. Soc. Rev.* **1972**, *1*, 337-353.

(2) Mitchell, P. R.; Parish, R. V. The eighteen electron rule. *J. Chem. Educ.* **1969**, *46*, 811.

(3) Wade, K. The structural significance of the number of skeletal bonding electron-pairs in carboranes, the higher boranes and borane anions, and various transition-metal carbonyl cluster compounds. *J. Chem. Soc. D: Chem. Commun.* **1971**, 792-793.

(4) Mingos, D. M. P. A General Theory for Cluster and Ring Compounds of the Main Group and Transition Elements. *Nat. Phys. Sci.* **1972**, *236*, 99-102.
(5) Kauzlarich, S. M. *Chemistry, structure, and bonding of Zintl phases and ions*; VCH Publishers, 1996.
(6) Scharfe, S.; Kraus, F.; Stegmaier, S.; Schier, A.; Fässler, T. F. Zintl ions, cage compounds, and intermetalloid clusters of Group 14 and Group 15 elements. *Angew. Chem. Int. Ed. Engl.* **2011**, *50*, 3630-3670.
(7) Zintl, E.; Dullenkopf, W. Ueber den Gitterbau von NaTl und seine Beziehung zu den Strukturen vom Typus des beta-Messings. *Z. Phys. Chem. B: Chemie der Elementarprozesse, Aufbau der Materie* **1932**, *16*, 195-205.
(8) Mizutani, U. *Hume-Rothery Rules for Structurally Complex Alloy Phases*; CRC Press: Boca Raton, FL, 2011.
(9) Mizutani, U.; Takeuchi, T.; Sato, H. Interpretation of the Hume–Rothery rule in complex electron compounds: γ-phase Cu_5Zn_8 Alloy, FK-type $Al_{30}Mg_{40}Zn_{30}$ and MI-type $Al_{68}Cu_7Ru_{17}Si_8$ 1/1–1/1–1/1 approximants. *Prog. Mater Sci.* **2004**, *49*, 227-261.
(10) Steinberg, S. Revisiting the frontier of the Zintl–Klemm approach for the examples of three Mo_2FeB_2-type intermetallics by means of quantumchemical techniques. *Z. Anorg. Allg. Chem.* **2023**, *649*, e202300113.
(11) Hafner, J. Structure, bonding, and stability of topologically close-packed intermetallic compounds. *Phys. Rev. B* **1977**, *15*, 617-630.
(12) Fredrickson, R. T.; Fredrickson, D. C. Chemical Pressure-Derived Assembly Principles for Dodecagonal Quasicrystal Approximants and Other Complex Frank–Kasper Phases. *Inorg. Chem.* **2022**, *61*, 17682-17691.
(13) Blatova, O. A.; Osipov, V. T.; Pavlova, V. E.; Solodovnikova, M. A.; Trofimychev, I. I.; Egorova, E. M.; Blatov, V. A. Local Atomic Configurations in Intermetallic Crystals: Beyond the First Coordination Shell. *Inorg. Chem.* **2023**, *62*, 6214-6223.
(14) Dominguez Montero, A.; McCandless, G. T.; Oladehin, O.; Baumbach, R. E.; Chan, J. Y. Development of a Geometric Descriptor for the Strategic Synthesis of Remeika Phases. *Chem. Mater.* **2023**, *35*, 2238-2247.
(15) Giaquinta, D. M.; zur Loye, H.-C. Structural Predictions in the ABO_3 Phase Diagram. *Chem. Mater.* **1994**, *6*, 365-372.
(16) van Vucht, J. H. N.; Buschow, K. H. J. On binary aluminium-rich compounds of the rare earth elements. *Philips Res. Rep.* **1964**, *19*, 319-322.
(17) van Vucht, J. H. N. Influence of radius ratio on the structure of intermetallic compounds of the AB_3 type. *J. Less-Common Met.* **1966**, *11*, 308-322.
(18) Villars, P. A three-dimensional structural stability diagram for 998 binary AB intermetallic compounds. *J. Less Common Met.* **1983**, *92*, 215-238.
(19) Peterson, G. G. C.; Geisler, E. E.; Fredrickson, D. C. Intermetallic Reactivity: $Ca_3Cu_{7.8}Al_{26.2}$ and the Role of Electronegativity in the Stabilization of Modular Structures. *Inorg. Chem.* **2020**, *59*, 5018-5029.
(20) Lin, Q.; Miller, G. J. Electron-Poor Polar Intermetallics: Complex Structures, Novel Clusters, and Intriguing Bonding with Pronounced Electron Delocalization. *Acc. Chem. Res.* **2018**, *51*, 49-58.
(21) Hume-Rothery, W. *The Structure of Metals and Alloys*; The Institute of Metals: London, 1950.
(22) Yannello, V. J.; Fredrickson, D. C. Generality of the 18-*n* Rule: Intermetallic Structural Chemistry Explained through Isolobal Analogies to Transition Metal Complexes. *Inorg. Chem.* **2015**, *54*, 11385-11398.
(23) Lim, A.; Fredrickson, D. C. Entropic Control of Bonding, Guided by Chemical Pressure: Phase Transitions and 18-*n*+*m* Isomerism of $IrIn_3$. *Inorg. Chem.* **2023**, *62*, 10833-10846.
(24) Iwasaki, Y.; Kimura, K.; Kitahara, K. Three-Center Bonds in an Al–Pd–Co Quasicrystalline Approximant: Wannier Function-Based Chemical Bonding Analysis. *J. Phys. Chem. C* **2023**, *127*, 20945-20950.
(25) Likhanov, M. S.; Sytov, N. V.; Wei, Z.; Dikarev, E. V.; Shevelkov, A. V. Nowotny Chimney Ladder Phases with Group 5 Metals: Crystal and Electronic Structure and Relations to the $CrSi_2$ Structure Type. *Crystals* **2020**, *10*, 670.
(26) Yannello, V. J.; Fredrickson, D. C. Orbital Origins of Helices and Magic Electron Counts in the Nowotny Chimney Ladders: the 18 – *n* Rule and a Path to Incommensurability. *Inorg. Chem.* **2014**, *53*, 10627-10631.
(27) Verchenko, V. Y.; Wei, Z.; Tsirlin, A. A.; Callaert, C.; Jesche, A.; Hadermann, J.; Dikarev, E. V.; Shevelkov, A. V. Crystal Growth of the Nowotny Chimney Ladder Phase Fe2Ge3: Exploring New Fe-Based Narrow-Gap Semiconductor with Promising Thermoelectric Performance. *Chem. Mater.* **2017**, *29*, 9954-9963.
(28) Lu, E.; Fredrickson, D. C. Templating Structural Progessions in Intermetallics: How Chemical Pressure Directs Helix Formation in the Nowotny Chimney Ladders. *Inorg. Chem.* **2019**, *58*, 4063-4066.
(29) Likhanov, M. S.; Verchenko, V. Y.; Gippius, A. A.; Zhurenko, S. V.; Tkachev, A. V.; Wei, Z.; Dikarev, E. V.; Kuznetsov, A. N.; Shevelkov, A. V. Electron-Precise Semiconducting $ReGa_2Ge$: Extending the $IrIn_3$ Structure Type to Group 7 of the Periodic Table. *Inorg. Chem.* **2020**, *59*, 12748-12757.
(30) Verchenko, V. Y.; Zubtsovskii, A. O.; Tsirlin, A. A.; Shevelkov, A. V. Chemical pressure in the correlated narrow-gap semiconductor FeGa3. *J. Mater. Sci.* **2019**, *54*, 2371-2378.
(31) Mitchell Warden, H. E.; Fredrickson, D. C. Frustrated and Allowed Structural Transitions: The Theory-Guided Discovery of the Modulated Structure of IrSi. *J. Am. Chem. Soc.* **2019**, *141*, 19424-19435.
(32) Lim, A.; Hilleke, K. P.; Fredrickson, D. C. Emergent Transitions: Discord between Electronic and Chemical Pressure Effects in the $REAl_3$ (*RE* = Sc, Y, Lanthanides) Series. *Inorg. Chem.* **2023**, *62*, 4405-4416.
(33) Hellner, E. Flußspat-Misch-Typen[1]. *Z. Kristallogr.* **1956**, *107*, 99-123.
(34) Künnen, B.; Niepmann, D.; Jeitschko, W. Structure refinements and some properties of the transition metal stannides Os3Sn7, Ir5Sn7, Ni0.402(4)Pd0.598Sn4, α-PdSn2 and PtSn4. *J. Alloys Compd.* **2000**, *309*, 1-9.
(35) Nylén, J.; Garcìa Garcìa, F. J.; Mosel, B. D.; Pöttgen, R.; Häussermann, U. Structural relationships, phase stability and bonding of compounds $PdSn_n$ (n=2, 3, 4). *Solid State Sci.* **2004**, *6*, 147-155.
(36) Schubert, K.; Pfisterer, H. Zur Kristallchemie der B-Metall-reichsten Phasen in in Legierungen von Uebergangsmetallen der Eisen- und Platintriaden mit Elementen der vierten Nebengruppe. *Z. Metallkd.* **1950**, *41*, 433-441.
(37) Kresse, G.; Hafner, J. Ab initio molecular dynamics for liquid metals. *Phys. Rev. B* **1993**, *47*, 558-561.
(38) Kresse, G.; Furthmüller, J. Efficient iterative schemes for ab initio total-energy calculations using a plane-wave basis set. *Phys. Rev. B* **1996**, *54*, 11169-11186.
(39) Kresse, G.; Furthmüller, J. Efficiency of ab-initio total energy calculations for metals and semiconductors using a plane-wave basis set. *Comput. Mater. Sci.* **1996**, *6*, 15-50.
(40) Blöchl, P. E. Projector Augmented-wave Method. *Phys. Rev. B* **1994**, *50*, 17953-17979.
(41) Kresse, G.; Joubert, D. From ultrasoft pseudopotentials to the projector augmented-wave method. *Phys. Rev. B* **1999**, *59*, 1758-1775.
(42) Lim, A.; Flores, B.; Fredrickson, D. C. 2024. DFT-raMO.jl, a Julia program for raMO analysis. This package is freely available at URL: https://github.com/xamberl/DFT-raMO [last accessed: Mar. 19, 2024]
(43) Yannello, V. J.; Lu, E.; Fredrickson, D. C. At the Limits of Isolobal Bonding: π-Based Covalent Magnetism in Mn_2Hg_5. *Inorg. Chem.* **2020**, *59*, 12304-12313.
(44) Gonze, X.; Amadon, B.; Anglade, P. M.; Beuken, J. M.; Bottin, F.; Boulanger, P.; Bruneval, F.; Caliste, D.; Caracas, R.; Côté, M.; Deutsch, T.; Genovese, L.; Ghosez, P.; Giantomassi, M.; Goedecker, S.; Hamann, D. R.; Hermet, P.; Jollet, F.; Jomard, G.; Leroux, S.; Mancini, M.; Mazevet, S.; Oliveira, M. J. T.; Onida, G.; Pouillon, Y.; Rangel, T.; Rignanese, G. M.; Sangalli, D.; Shaltaf, R.; Torrent, M.; Verstraete, M. J.; Zerah, G.; Zwanziger, J. W. ABINIT: First-principles approach to material and nanosystem properties. *Comput. Phys. Commun.* **2009**, *180*, 2582-2615.
(45) Gonze, X.; Rignanese, G.-m.; Verstraete, M.; Beuken, J.-m.; Pouillon, Y.; Caracas, R.; Raty, J.-y.; Olevano, V.; Bruneval, F.; Reining, L.; Godby, R.; Onida, G.; Hamann, D. R.; Allan, D. C. A brief introduction to the ABINIT software package. *Z. Kristallogr. - Cryst. Mater.* **2005**, *220*, 558-562.
(46) Gonze, X.; Beuken, J. M.; Caracas, R.; Detraux, F.; Fuchs, M.; Rignanese, G. M.; Sindic, L.; Verstraete, M.; Zerah, G.; Jollet, F.; Torrent, M.; Roy, A.; Mikami, M.; Ghosez, P.; Raty, J. Y.; Allan, D. C. First-principles computation of material properties: the ABINIT software project. *Comput. Mater. Sci.* **2002**, *25*, 478-492.
(47) Gonze, X.; Jollet, F.; Abreu Araujo, F.; Adams, D.; Amadon, B.; Applencourt, T.; Audouze, C.; Beuken, J. M.; Bieder, J.; Bokhanchuk, A.; Bousquet, E.; Bruneval, F.; Caliste, D.; Côté, M.; Dahm, F.; Da Pieve, F.; Delaveau, M.; Di Gennaro, M.; Dorado, B.; Espejo, C.; Geneste, G.; Genovese, L.; Gerossier, A.; Giantomassi, M.; Gillet, Y.; Hamann, D. R.; He, L.; Jomard, G.; Laflamme Janssen, J.; Le Roux, S.; Levitt, A.; Lherbier, A.; Liu, F.; Lukačević, I.; Martin, A.; Martins, C.; Oliveira, M. J. T.; Poncé, S.; Pouillon, Y.; Rangel, T.; Rignanese, G. M.; Romero, A. H.; Rousseau, B.; Rubel, O.; Shukri, A. A.; Stankovski, M.; Torrent, M.; Van Setten, M. J.; Van Troeye, B.; Verstraete, M. J.; Waroquiers, D.; Wiktor, J.; Xu, B.; Zhou, A.; Zwanziger, J. W. Recent

developments in the ABINIT software package. *Comput. Phys. Commun.* **2016**, *205*, 106-131.
(48) Hartwigsen, C.; Goedecker, S.; Hutter, J. Relativistic separable dual-space Gaussian pseudopotentials from H to Rn. *Phys. Rev. B* **1998**, *58*, 3641-3662.
(49) Sanders, K. M.; Van Buskirk, J. S.; Hilleke, K. P.; Fredrickson, D. C. Self-Consistent Chemical Pressure Analysis: Resolving Atomic Packing Effects through the Iterative Partitioning of Space and Energy. *J. Chem. Theory Comput.* **2023**, *19*, 4273-4285.
(50) Hilleke, K. P.; Fredrickson, D. C. Discerning Chemical Pressure Amidst Weak Potentials: Vibrational Modes and Dumbbell/Atom Substitution in Intermetallic Aluminides. *J. Phys. Chem. A* **2018**, *122*, 8412-8426.
(51) Oliveira, M. J. T.; Nogueira, F. Generating relativistic pseudo-potentials with explicit incorporation of semi-core states using APE, the Atomic Pseudo-potentials Engine. *Comput. Phys. Commun.* **2008**, *178*, 524-534.
(52) Berns, V. M.; Engelkemier, J.; Guo, Y.; Kilduff, B. J.; Fredrickson, D. C. Progress in Visualizing Atomic Size Effects with DFT-Chemical Pressure Analysis: From Isolated Atoms to Trends in AB_5 Intermetallics. *J. Chem. Theory. Comput.* **2014**, *10*, 3380-3392.
(53) Siggelkow, L.; Hlukhyy, V.; Fässler, T. F. Crystal Structure of $Mg_{0.39(2)}NiSn_{1.61(2)}$ and $Mg_{2.61(2)}Ni_4Sn_{3.39(2)}$ Featuring Mg/Sn Atom Networks with Different Connections of $Ni@(Mg/Sn)_8$ Coordination Polyhedra. *Z. Anorg. Allg. Chem.* **2015**, *641*, 221-228.
(54) Häussermann, U.; Landa-Cánovas, A. R.; Lidin, S. The Phase $Co_{1-x}Ni_xSn_2$: Structural Variations Based on the Stacking of Two Different Planar Nets. *Inorg. Chem.* **1997**, *36*, 4307-4315.
(55) Flandorfer, H.; Richter, K. W.; Giester, G.; Ipser, H. The Ternary Compounds $Pd_{13}In_{5.25}Sb_{3.75}$ and $PdIn_{1.26}Sb_{0.74}$: Crystal Structure and Electronic Structure Calculations. *J. Solid State Chem.* **2002**, *164*, 110-118.
(56) El-Boragy, M.; Schubert, K. Kristallstrukturen einiger ternärer Phasen in T-B-B'-Systemen. *Z. Metallkd.* **1971**, *62*, 667-675.
(57) Sarah, N.; Rajasekharan, T.; Schubert, K. Über die Mischung $NiZn_M$ $Ge_{M'}$. *Z. Metallkd.* **1981**, *72*, 652-656.
(58) Chang, C. C.; Hsu, C. E.; Haung, J. Y.; Liu, T. C.; Cheng, C. M.; Chen, W. T.; Cheng, P. Y.; Kuo, C. N.; Lue, C. S.; Lee, C. C.; Huang, C. L. Electrical transport and electronic properties of multiband metallic $PdSn_2$. *Phys. Rev. B* **2023**, *108*, 205133.
(59) Wang, F.; Miller, G. J. Revisiting the Zintl–Klemm Concept: Alkali Metal Trielides. *Inorg. Chem.* **2011**, *50*, 7625-7636.
(60) Sánchez-Portal, D.; Martin, R. M.; Kauzlarich, S. M.; Pickett, W. E. Bonding, moment formation, and magnetic interactions in $Ca_{14}MnBi_{11}$ and $Ba_{14}MnBi_{11}$. *Phys. Rev. B* **2002**, *65*, 144414.
(61) Boulet, P.; de Weerd, M.-C.; Gaudry, E.; Šturm, S.; Zollinger, J.; Dubois, J.-M.; Fournée, V.; Ledieu, J. Al_4Ir: An Al–Ir Binary-Phase Superstructure of the Ni_2Al_3 Type. *Inorg. Chem.* **2022**, *61*, 8823-8833.
(62) Wannier, G. H. The Structure of Electronic Excitation Levels in Insulating Crystals. *Phys. Rev.* **1937**, *52*, 191-197.
(63) Marzari, N.; Mostofi, A. A.; Yates, J. R.; Souza, I.; Vanderbilt, D. Maximally Localized Wannier functions: Theory and Applications. *Rev. Mod. Phys.* **2012**, *84*, 1419-1475.
(64) An example of the importance of the order of the raMO reconstructions can be found in Ref. 43. In cases where the desired functions have similar energies or degrees of localization, some trial and error is necessary.
(65) Nelson, D. R. Order, frustration, and defects in liquids and glasses. *Phys. Rev. B* **1983**, *28*, 5515-5535.

For Table of Contents Use Only

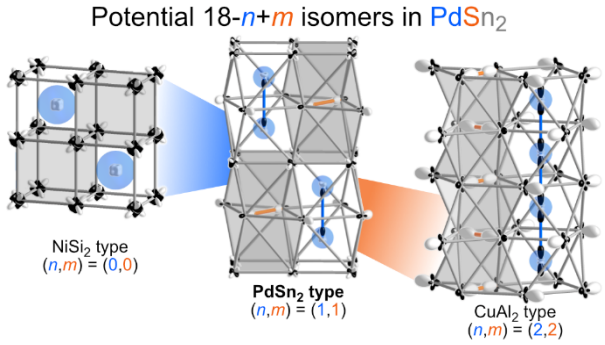

Synopsis: We explore the driving forces stabilizing one 18-n+m isomer over another in $PdSn_2$. The DFT-reversed approximation MO method establishes that $PdSn_2$ and its hypothetical parent structures can be regarded as 18-n+m isomers. DFT-Chemical Pressure analysis reveals how the observed $PdSn_2$ structure balances the conflicting requirements of Sn-Sn clustering and expansion of the Pd environment, and points to generalizations where increased main group ligand clustering $(+m)$ and isolobal bonds $(+n)$ can accommodate different atomic space requirements.